ACS OMEGA

Open Access

http://pubs.acs.org/journal/acsodf

Article

Ru-Doped Co_3O_4 Nanoparticles as Efficient and Stable Electrocatalysts for the Chlorine Evolution Reaction

Won Il Choi, Seungwoo Choi, Mani Balamurugan, Sunghak Park, Kang Hee Cho, Hongmin Seo, Heonjin Ha, and Ki Tae Nam*

Cite This: *ACS Omega* 2023, 8, 35034−35043

Read Online

ACCESS | Metrics & More | Article Recommendations | Supporting Information

ABSTRACT: The electrochemical chlorine evolution reaction (CER) is one of the most important electrochemical reactions. Typically, iridium (Ir)- or ruthenium (Ru)-based mixed metal oxides have been used as electrocatalysts for the CER due to their high activities and durabilities. However, the scarcity of Ir and Ru has indicated the need to develop alternative earth-abundant transition-metal-based CER catalysts. In this study, we report a Co_3O_4 nanoparticle (NP) catalyst synthesized by a hydrothermal method. Furthermore, Ru was successfully incorporated into the Co_3O_4 NPs ($Ru_xCo_{3-x}O_4$ NPs) for further improvement of catalytic performance in chlorine generation. Electrokinetic analyses combined with in situ X-ray absorption near-edge structure (XANES) results suggested an identical CER mechanism for the Co_3O_4 NPs and $Ru_xCo_{3-x}O_4$ NPs. Various characterization techniques demonstrated that the homogeneous substitution of Ru^{4+} ions into the Co^{3+} octahedral sites enhanced the structural disorder and changed the electronic state of Co_3O_4, resulting in additional exposed active sites. Remarkably, the $Ru_{0.09}Co_{2.91}O_4$ NP electrode exhibited outstanding stability for more than 150 h even at a high current density of 500 mA/cm^2, which shows its commercial viability for active chlorine generation.

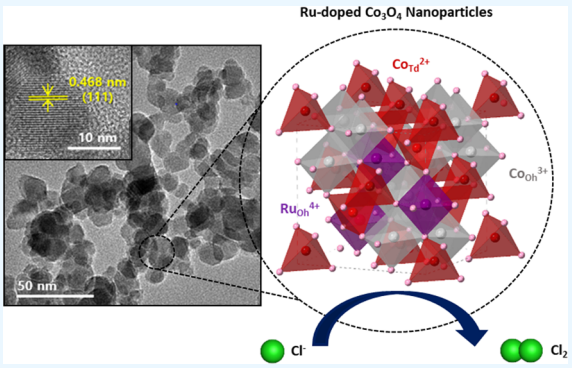

1. INTRODUCTION

Chlorine (Cl_2) has been extensively used as a basic chemical in the production of polymers, pharmaceuticals, and dyes.[1] Currently, most of the chlorine has been produced by a chlor-alkali process that entails the chlorine evolution reaction (CER) in conjunction with the hydrogen evolution reaction (HER), and over 150 TWh of electric energy is consumed annually by this process.[2] In addition to gaseous chlorine, active chlorine (AC), which consists of hypochlorous acid (HClO) and hypochlorite ions (ClO^-) generated during the CER, is important for wastewater and ballast water treatment as it effectively removes harmful organisms causing ecological problems.[3] A rational design of highly efficient, selective, and durable anodes is crucial to address the energy challenges because the electrode materials mainly determine the chlorine yield and the overall power consumption of the system.[4,5] Dimensionally stable anodes (DSAs) consisting of iridium (Ir)- and ruthenium (Ru)-based mixed metal oxides (MMOs) have been most widely used as industrial CER catalysts due to their low overpotentials and high stabilities in the CER.[6,7] However, the requirement of high noble metal contents (at least 30 atom %) has been considered a challenge to overcome.[8,9] Therefore, developing earth-abundant metal-based CER catalysts with high catalytic activities and stabilities is highly desirable.

In this respect, several nonprecious metal oxide-based catalysts and single-atom catalysts, such as transition-metal antimonates, Ti−V−Sn−Sb-oxide, Co_3O_4 nanoarrays, and Pt−N_4 site-doped carbon nanotubes (Pt_1/CNTs), have been explored as alternative CER catalysts.[10−13] However, the aforementioned materials exhibited limited stabilities far lower than those of industrially available catalysts, which constrain scalable application. Furthermore, the mechanistic understanding of the CER with these materials has remained unclear. Investigation of the detailed reaction kinetics and verification of the rate-determining step (RDS) are important research directions required for a fundamental understanding of the catalytic characteristics and the design of efficient and selective electrocatalysts.[14] Recently, our group reported monodisperse Co_3O_4 nanoparticles (NPs) coated on a fluorine-doped tin oxide (FTO) anode as an earth-abundant transition-metal-based CER catalyst synthesized by the hot-injection method.[15] It showed a high CER performance and selectivity under neutral pH. Furthermore, based on electrokinetic and spectroscopic analyses, a chlorine-evolving mechanism was proposed for the Co_3O_4 NPs. However,

Received: June 25, 2023
Accepted: August 31, 2023
Published: September 13, 2023

efforts to achieve practical utility with the Co_3O_4 NPs, such as improving the stability under high anodic potential and overcoming the sluggish reaction kinetics, have not been addressed.

Heteroatom engineering has been widely employed to tune the coordination environments and electronic structures of transition-metal-oxide (TMO) catalysts, thereby enhancing their intrinsic catalytic properties.[16−19] Based on this principle, several attempts have been made to incorporate secondary metal atoms into the spinel Co_3O_4 lattice and control the populations of the tetrahedral Co^{2+} and octahedral Co^{3+} sites, which led to surface reconstruction and tuning of the adsorption capacities of intermediates.[20−23] As proven by theoretical calculations and spectroscopic results, Ru has optimal adsorption energies for the intermediates of various oxidation processes.[24,25] The substituted Ru species hasten electron transfer and provide oxygen vacancies and exposed active sites, thus accelerating the overall reaction kinetics.[26,27] Specifically, Qi et al. fabricated inter-doped $(Ru−Co)O_x$ nanosheet arrays as efficient bifunctional catalysts for overall water splitting. The enhanced activity was attributed to the heterogeneous interfacial electronic interaction of Co and Ru, as well as to the enlarged active surface area resulting from Ru doping.[28] Additionally, Ru doping plays an important role in improving the electrical conductivity and lowering the charge-transfer resistance.[29] However, to date, a comprehensive study of Ru-doped CER electrocatalysts encompassing a microscopic mechanistic understanding, as well as evaluations of the electrochemical stability under commercial level of current density, has not been explored.

Herein, we designed and fabricated Co_3O_4 NPs via a facile and scalable hydrothermal method and incorporated Ru into the Co_3O_4 NPs by mixing them with a Ru precursor followed by thermal annealing. Comprehensive characterization, including X-ray diffraction (XRD), X-ray photoelectron spectroscopy (XPS), and transmission electron microscopy (TEM) analyses, demonstrated that the Ru^{4+} ions were uniformly incorporated in the octahedral Co^{3+} sites, resulting in changes in the electronic state and distortion of the Co_3O_4 crystal structure. The $Ru_{0.09}Co_{2.91}O_4$ NPs exhibited superior CER activity compared to RuO_2 and commercial DSA under neutral brine condition. In addition, by combining electrokinetic and in situ X-ray absorption near-edge structure (XANES) analyses, the chlorine evolution mechanism for the Co_3O_4 NPs and $Ru_xCo_{3-x}O_4$ NPs was proposed. The enhanced catalytic performance was attributed to the highly active Ru dopants located at the octahedral sites and the additional active sites caused by the structural disorder. Notably, $Ru_{0.09}Co_{2.91}O_4$ NPs deposited on a titanium (Ti) substrate showed a lifetime of over 150 h at a current density of 500 mA/cm^2, which was ten times longer than that of the RuO_2 anode.

2. EXPERIMENTAL SECTION

2.1. Hydrothermal Synthesis of Co_3O_4 NPs. Hydrothermal Co_3O_4 (HT-Co_3O_4) NPs were synthesized by modifying the hydrothermal synthetic process reported previously.[30,31] Cobalt(II) acetate tetrahydrate (1 g) was dissolved in ethanol (50 mL) under 45 °C for 10 min, and ammonium hydroxide (6.6 mL) was added dropwise under vigorous stirring. Then, the solution was transferred into a Teflon-lined autoclave and held at 150 °C for 3 h. Afterward, acetone (200 mL) was added to the crude solution, followed by centrifugation at 13,500 rpm for 20 min. The precipitated products were dispersed in methanol (24 mL), and the washing procedure was repeated by adding acetone and centrifugation. The final HT-Co_3O_4 NP product was stored in ethanol (2 mL).

2.2. Ruthenium Treatment of the HT-Co_3O_4 NPs and Electrode Preparation. The HT-Co_3O_4 NPs were purified by mixing the HT-Co_3O_4 NP product (20 μL) and acetone (1 mL), followed by centrifugation at 13,500 rpm for 3 min. For ruthenium incorporation into the HT-Co_3O_4 NPs, ruthenium(III) acetylacetonate was dispersed in ethanol with a molar ratio of Ru/(Co + Ru) from 0 to 10 atom %. Then, the Co_3O_4 NP precipitate was homogeneously dispersed with the as-prepared ruthenium(III) acetylacetonate solution (20 μL). The final dispersed product was drop-coated on a Ti plate or an FTO substrate over an area of 0.5 cm^2. Afterward, heat treatment was conducted at 300 °C for 1 h. In the case of an electrode designed for lifetime measurements, ruthenium(III) acetylacetonate was dispersed in a mixture of isopropyl alcohol (IPA) and water with a volume ratio of 85:15, followed by homogeneous mixing with the precipitated Co_3O_4 NPs. Then, the mixture solution was brush-coated on the Ti substrate and dried at 500 °C for 5 min. This process was repeated 10 times. Finally, the coated electrode underwent thermal annealing at 500 °C for 1 h.

2.3. Synthesis of the RuO_2 Electrode. The RuO_2 electrode was prepared by modifying the previous thermal decomposition method.[12,32] A 10 mM $RuCl_3$ solution in a mixed solvent with a 1:19 volume ratio of water and ethanol was drop-coated on the Ti plate substrate, followed by annealing at 300 °C for 1 h. For an electrode designed for lifetime measurements, layer-by-layer brush-coating and a 500 °C for 1 h annealing process were applied as described for the $Ru_xCo_{3-x}O_4$ NP electrode.

2.4. Material Characterization. The surface morphology of the $Ru_xCo_{3-x}O_4$ NP electrode was characterized using a field-emission scanning electron microscope (SEM; Model: SUPRA 55VP, Carl Zeiss, Germany) with an acceleration voltage of 2 kV. The morphology and electron diffraction pattern were determined by field-emission TEM (JEM-2100F, JEOL, Japan) with an accelerating voltage of 200 kV. The TEM samples were prepared by blading the electrode surface and dispersing the peeled off particles with ethanol, followed by dropping them onto the TEM grid. The XRD patterns were obtained using a high-resolution X-ray diffractometer (SmartLab, Rigaku, Japan) equipped with Cu Kα radiation (λ = 1.5406 Å) and measured over a 2θ range of 10−70° with step sizes of 0.02° and a scan rate of 1°/min. The surface characteristics of the HT-Co_3O_4 and $Ru_xCo_{3-x}O_4$ NPs were examined by XPS (K-alpha, Thermo Fisher Scientific). The obtained spectra were deconvoluted using CasaXPS software after a Shirley-type background correction. All of the binding energies in the XPS spectra were calibrated to the C 1s peak (284.8 eV). XANES measurements were carried out on a BL10C beamline at the Pohang Accelerator Laboratory (PLS II), Korea, with a ring current of 350 mA at an electron beam energy of 3.0 GeV. The spectra were measured in fluorescence mode at the Co K-edge region. The in situ potential-dependent XANES spectra were collected with an in situ electrochemical cell. Detailed electrochemical cell configurations were illustrated in our previous studies.[14,33] The contents of Co and Ru in the catalysts were analyzed by inductively coupled plasma mass spectrometry (ICP−MS; Model: 7900 ICP−MS, Agilent Technologies, Japan). The samples for

https://doi.org/10.1021/acsomega.3c04525
ACS Omega 2023, 8, 35034−35043

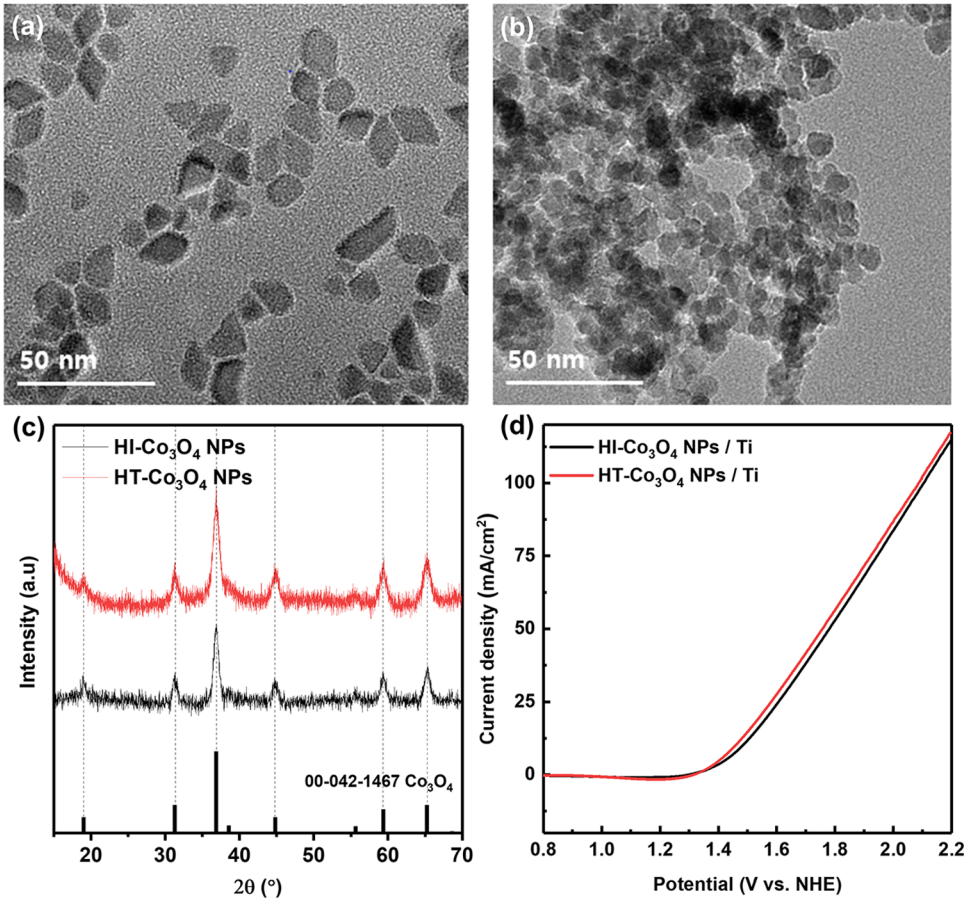

Figure 1. TEM images of (a) hot-injection Co_3O_4 (HI-Co_3O_4) NPs and (b) hydrothermal Co_3O_4 (HT-Co_3O_4) NPs. (c) XRD patterns of the HI-Co_3O_4 NPs and HT-Co_3O_4 NPs, respectively. (d) Polarization-corrected cyclic voltammetry (CV) curves of HI-Co_3O_4 NPs and HT-Co_3O_4 NPs under a neutral 0.6 M NaCl, respectively.

ICP−MS were prepared by fully dissolving the catalysts on the electrodes with hydrochloric acid.

2.5. Electrochemical Measurements. All of the electrochemical measurements except the long-term stability tests were conducted in a three-electrode system where a Pt foil and a Ag/AgCl/3 M KCl electrode were used as the counter electrode and reference electrode, respectively. All of the applied potentials were converted to the normal hydrogen electrode (NHE) scale with the following equation: E (vs NHE) = E (vs Ag/AgCl) + 0.205 V. All electrochemical experiments were carried out without iR correction. Cyclic voltammetry (CV) was performed with a scan rate of 50 mV s^{-1} with stirring. The polarization-corrected curves were obtained by averaging the current densities in the forward and backward scans. The Tafel slopes were obtained from the steady-state current densities by chronopotentiometry (CP). Long-term stability was measured with a two-electrode system in which a titanium mesh was used as a counter electrode.

2.6. Product Analysis. The *N,N*-diethyl-*p*-phenylenediamine (DPD) colorimetric method was used to quantify the active chlorine generated. A Pocket Colorimeter II and DPD reagents were purchased from Hach. A sample solution was prepared by extracting the electrolyte, which underwent 5 min of electrolysis at a certain current density followed by dilution at least 10 times.

3. RESULTS AND DISCUSSION

3.1. Synthesis of the HT-Co_3O_4 NPs. The HT-Co_3O_4 NPs were synthesized by modifying the hydrothermal process reported previously.[30,31,34] Additionally, monodispersed hot-injection Co_3O_4 (HI-Co_3O_4) NPs were prepared by thermal decomposition, as reported earlier.[15] As shown in the TEM images in Figure 1a,b, rhombic NPs with a diameter of 10−15 nm were obtained through the hot-injection method, and 8−12 nm-sized NPs were synthesized by the hydrothermal process. The XRD patterns for both the HI-Co_3O_4 NPs and HT-Co_3O_4 NPs showed no difference, and the peaks at 2θ = 19.0, 31.3, 36.9, 44.9, 59.5, and 65.4° corresponded to the (111), (220), (311), (400), (511), and (440) planes of cubic Co_3O_4 (JCPDS no. 00-042-1467) (Figure 1c). Furthermore, the Co 2p XPS spectra (Figure S1) showed identical surface chemical compositions and Co valence states for Co_3O_4 NPs prepared via different synthetic processes. The $Co2p_{3/2}$ and $Co2p_{1/2}$ binding energies for both the HI-Co_3O_4 NPs and HT-Co_3O_4 NPs were 794.72 and 779.78 eV, respectively, indicating a $Co2p_{3/2}$−$2p_{1/2}$ spin−orbital-level energy spacing of 15 eV, which is characteristic of Co_3O_4.[35] Films of HI-Co_3O_4 NPs and HT-Co_3O_4 NPs were prepared by arrangement onto a Ti plate by drop-coating and subsequent thermal annealing under air. Figure 1d illustrates the polarization-corrected CV curves of the HI-Co_3O_4 NPs and HT-Co_3O_4 NPs in neutral 0.6 M NaCl. The HT-Co_3O_4 NPs exhibited a

https://doi.org/10.1021/acsomega.3c04525
ACS Omega 2023, 8, 35034−35043

Table 1. Loading Amounts of Ru and Co and Compositions of the Resultant $Ru_xCo_{3-x}O_4$ Nanoparticle Samples According to the Reactant Molar Ratio Ru/(Co + Ru)

reactant molar ratio of Ru/(Co + Ru) [%]	Ru amount [mg/cm^2]	Co amount [mg/cm^2]	Ru content [atom %]	Co content [atom %]	stoichiometric Co/Ru	sample notation
1	0.013	1.071	0.69	99.31	143.92	$Ru_{0.02}Co_{2.98}O_4$
2	0.028	1.192	1.33	98.67	74.19	$Ru_{0.04}Co_{2.96}O_4$
5	0.068	1.229	3.13	96.87	30.95	$Ru_{0.09}Co_{2.91}O_4$
10	0.104	1.212	4.77	95.23	19.96	$Ru_{0.14}Co_{2.86}O_4$

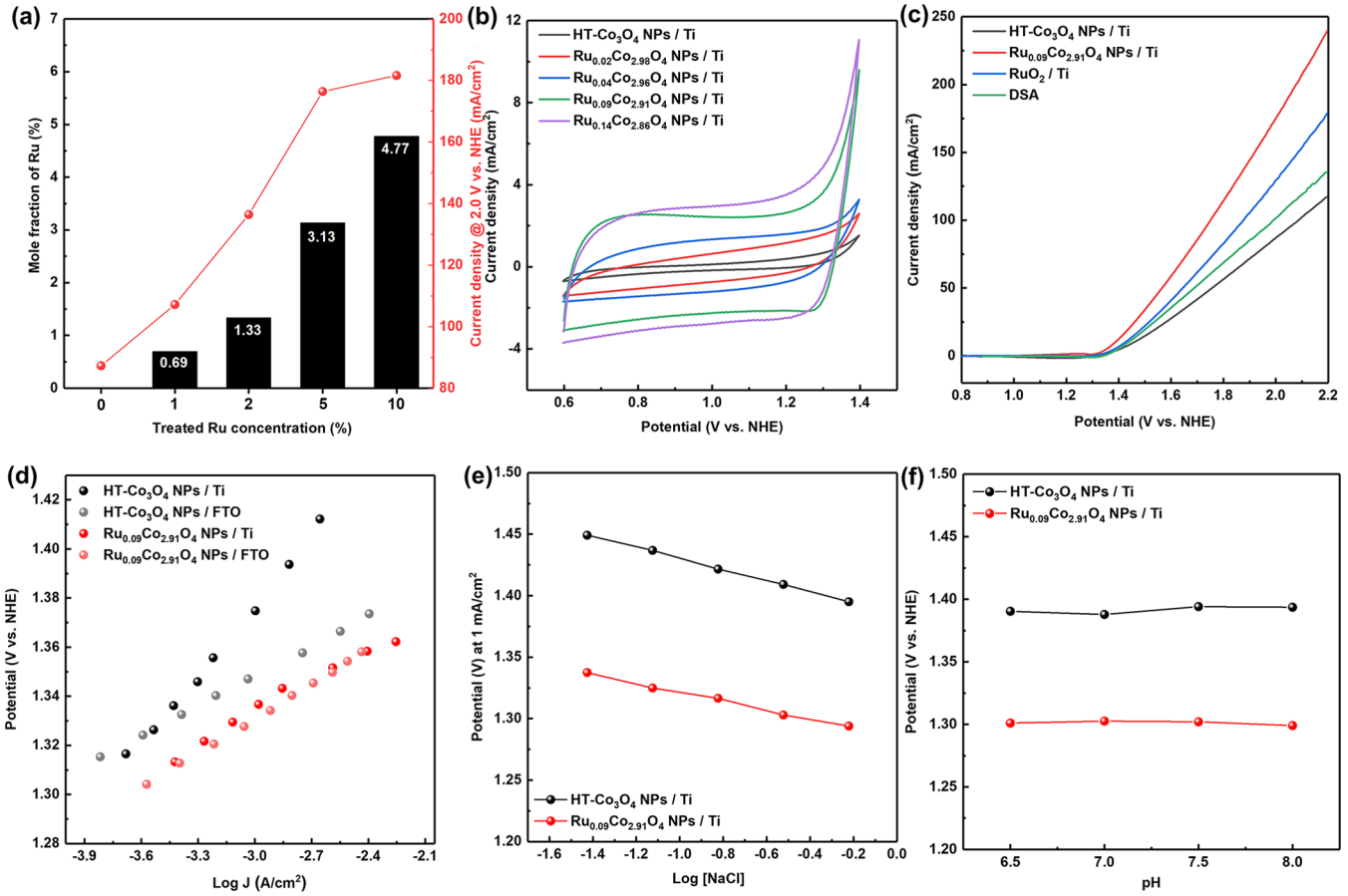

Figure 2. (a) Current densities generated at 2.0 V (vs NHE) (obtained from Figure S2) with the indicated Ru contents in $Ru_xCo_{3-x}O_4$ NP samples according to the Ru/(Co + Ru) molar ratio. (b) CV curves for the $Ru_xCo_{3-x}O_4$ NPs in 0.6 M NaCl. (c) Polarization-corrected CV curves for $Ru_{0.09}Co_{2.91}O_4$ NPs, hydrothermal Co_3O_4 (HT-Co_3O_4) NPs, the dimensionally stable anode (DSA), and RuO_2 in 0.6 M NaCl. (d) Tafel plots for HT-Co_3O_4 NPs and $Ru_{0.09}Co_{2.91}O_4$ NPs on titanium and FTO substrates (0.6 M NaCl). (e) Potentials required to reach 1 mA/cm^2 with HT-Co_3O_4 NPs and $Ru_{0.09}Co_{2.91}O_4$ NPs under various chloride concentrations. (f) pH dependence of the potentials for the HT-Co_3O_4 NPs and $Ru_{0.09}Co_{2.91}O_4$ NPs over the neutral pH range in 0.6 M NaCl.

slightly higher catalytic performance than the HI-Co_3O_4 NPs, which was attributed to the relatively smaller particle sizes.

These characterization results showed that the Co_3O_4 NPs prepared via the two different synthetic methods were identical in terms of their structural properties, electronic structures, and electrochemical activities. Based on the scalability and commercial feasibility, in further development, the hydrothermal method was applied to the synthesis of Co_3O_4 NPs, which is a more facile and environmentally friendly method compared to the hot-injection synthetic process.

3.2. Synthesis and Electrochemical Analysis of the $Ru_xCo_{3-x}O_4$ NPs. Based on the principle of heteroatom engineering with Co_3O_4 and the Ru incorporation effect, we attempted to design a highly efficient and durable catalyst for the CER. A Ru treatment of the Co_3O_4 NPs ($Ru_xCo_{3-x}O_4$ NPs) was accomplished by mixing the as-prepared HT-Co_3O_4 NPs and a Ru precursor dissolved in ethanol followed by thermal annealing. A series of $Ru_xCo_{3-x}O_4$ NP samples was prepared by adjusting the reactant molar ratio Ru/(Co + Ru) to 1−10% during Ru treatment of the HT-Co_3O_4 NPs. The stoichiometries of the samples were determined by ICP−MS analyses (Table 1).

The electrochemical performance of $Ru_xCo_{3-x}O_4$ NPs was evaluated with polarization-corrected CV curves generated in a neutral 0.6 M NaCl solution (Figure S2). Figure 2a shows the relationship between the actual Ru content in the $Ru_xCo_{3-x}O_4$ NP catalysts, according to the intended Ru/(Co + Ru) reactant molar ratio, and the current density at 2.0 V (vs NHE). It was evident that the catalytic activity of the $Ru_xCo_{3-x}O_4$ NPs increased linearly up to a 3.13% Ru mole fraction ($Ru_{0.09}Co_{2.91}O_4$) but was saturated beyond that. Furthermore, the CV curves of $Ru_xCo_{3-x}O_4$ NPs at a scan

https://doi.org/10.1021/acsomega.3c04525
ACS Omega 2023, 8, 35034−35043

rate of 50 mV/s also showed a drastic enlargement of the integrated areas as the Ru content was increased up to the same point (Figure 2b). The increased level of charge accumulation was ascribed to the increase in the non-faradic electrochemical double-layer capacitance (C_{dl}) and pseudocapacitance characteristics. Indeed, it is well known that the combination of Ru-based materials with cobalt oxides leads to significant improvement of the supercapacitive properties by modulating the surface morphology and increasing the pseudocapacitance.[36−38] Additionally, the slope of anodic charging current density was also estimated by cyclic voltammetry at different scan rates. To exclude the contribution of the faradaic reaction, the potential range was set to ±50 mV around the open-circuit potential (OCP).[39] As shown in Figure S3, the average slope of the anodic charging current density of $Ru_{0.09}Co_{2.91}O_4$ NPs increased sharply up to 11.43 mF/cm^2, which was approx. 237 times larger than that of the HT-Co_3O_4 NPs (0.0483 mF/cm^2). The aforementioned electrochemical measurements clearly indicate that the CER activity and the capacitance of the $Ru_xCo_{3-x}O_4$ NPs were not predominantly determined by the Ru content of the $Ru_xCo_{3-x}O_4$ NPs and were possibly due to favorable interactions between Co and Ru. We examined the catalytic activities of the HT-Co_3O_4 NPs and $Ru_{0.09}Co_{2.91}O_4$ NPs and compared them with those of RuO_2 and a commercial DSA electrode. Figure 2c shows that even with smaller Ru contents, the $Ru_{0.09}Co_{2.91}O_4$ NPs exhibited superior activity compared to other Ru-based CER catalysts. Figure S4 illustrates the current efficiencies for chlorine generation by the HT-Co_3O_4 NPs, $Ru_{0.09}Co_{2.91}O_4$ NPs, and RuO_2 quantified by DPD colorimetry. The $Ru_{0.09}Co_{2.91}O_4$ NPs exhibited slightly higher selectivity than the HT-Co_3O_4 NPs and RuO_2, with efficiencies above 85% obtained with various current densities ranging from 5 to 500 mA/cm^2.

We conducted an electrokinetic investigation of the $Ru_{0.09}Co_{2.91}O_4$ NPs and compared them with the HT-Co_3O_4 NPs. The Tafel plots for the HT-Co_3O_4 NPs and $Ru_{0.09}Co_{2.91}O_4$ NPs were derived with an FTO substrate in addition to the Ti plate to exclude the effects of the charge-transfer limit at the interface between the substrate and catalysts. The Tafel slopes for the HT-Co_3O_4 NPs and $Ru_{0.09}Co_{2.91}O_4$ NPs on a Ti electrode were estimated as 85 and 41 mV/dec, respectively. In the FTO substrate, while the Tafel slope of $Ru_{0.09}Co_{2.91}O_4$ remained unchanged, that of the HT-Co_3O_4 NPs decreased significantly to 42 mV/dec (Figure 2d). Previous studies suggested that charge transfer at the interface between a catalyst film and the underlying substrate significantly affects the catalytic activity.[40] In particular, unlike highly conductive noble metal-based metallic oxides, earth-abundant metal oxides such as Co_3O_4 exhibit high interfacial resistance,[41,42] and the overall electrochemical performance is determined by the sluggish interfacial charge transport. In addition, in the Ti substrate, it is well known that the conductivity drops significantly due to the formation of an insulating TiO_2 layer at high annealing temperature. Taking this into account, the Tafel slope of the HT-Co_3O_4 NPs/Ti was thought to be affected by external constraints, and the Tafel slope reflecting the intrinsic reaction kinetics was regarded as that of Co_3O_4 NPs/FTO. The Tafel slope analysis of $Ru_{0.09}Co_{2.91}O_4$ demonstrated that a high conductivity that overcame the interfacial resistance was achieved with small amounts of Ru since the slopes were the same for both substrates. Theoretically, the Tafel slope (b) can be calculated from the relationship between the current density (j) and the potential (E) (eqs 1 and 2), where j_0, α, F, E^0, R, and T are the exchange current density, transfer coefficient, Faraday constant, thermodynamic equilibrium potential, gas constant, and temperature, respectively.[43] The Tafel slopes of 40−45 mV/dec correspond to a transfer coefficient (α) of 1.5, indicating that the second discharging process after the reversible one-electron transfer is the rate-determining step (RDS).

$$j = j_0 \exp\left(-\frac{\alpha F(E - E^0)}{RT}\right) \tag{1}$$

$$b = \frac{\partial E}{\partial \log j} = \frac{2.303RT}{\alpha F} \tag{2}$$

As illustrated in Figure 2e, the slopes of the potentials required to reach 1 mA/cm^2 with the different chloride concentrations were estimated to be −44 and −38 mV/dec for the HT-Co_3O_4 NPs and $Ru_{0.09}Co_{2.91}O_4$ NPs, respectively. Thus, taking together the value of the Tafel slope and the chloride concentration-dependent potential changes, the reaction order with respect to the chloride concentration was calculated to be unity for both the HT-Co_3O_4 NPs and the $Ru_{0.09}Co_{2.91}O_4$ NPs from eq 3. The first reaction order on the chloride concentration implies that discharge of a chloride ion occurred only once in the RDS or prior to the RDS.

$$\left(\frac{\partial E}{\partial \log[Cl^-]}\right)_j = -\left(\frac{\partial \log j}{\partial \log[Cl^-]}\right)_E \left(\frac{\partial E}{\partial \log j}\right)_{[Cl^-]} \tag{3}$$

Furthermore, the pH dependences on the HT-Co_3O_4 NPs and $Ru_{0.09}Co_{2.91}O_4$ NPs were measured under neutral conditions, which resulted in a zeroth order for both cases, as depicted in Figure 2f, demonstrating that the proton does not participate in the catalytic cycle for either the HT-Co_3O_4 NPs or the $Ru_{0.09}Co_{2.91}O_4$ NPs. On the basis of the overall electrokinetic results, an electrochemical rate law was derived for the HT-Co_3O_4 NPs and $Ru_xCo_{3-x}O_4$ NPs, in which k_0 and a_{Cl^-} are the rate constant and the activity of the chloride ions, respectively.

$$j = k_0 a_{Cl^-} \exp\left(\frac{1.5FE}{RT}\right) \tag{4}$$

As shown in eq 4, we revealed identical mechanistic behavior in the CER for the HT-Co_3O_4 NPs and $Ru_xCo_{3-x}O_4$ NPs, where the second electron transfer proceeds as the RDS following a reversible one-electron transfer process.

3.3. In Situ XANES Analysis of the $Ru_xCo_{3-x}O_4$ NPs. We investigated the oxidation-state variation of Co under an applied potential by in situ XANES to gain a detailed understanding of the mechanistic behavior of the HT-Co_3O_4 NPs and $Ru_{0.09}Co_{2.91}O_4$ NPs. The average Co oxidation state was estimated with the Co K-edge spectra of reference Co oxide materials for which the oxidation states were well known. The oxidation states under OCP, where external anodic bias is absent, were calculated to be 2.73 and 2.57 in the HT-Co_3O_4 NPs and $Ru_{0.09}Co_{2.91}O_4$, NPs, respectively, which matched the Co 2p XPS result, as will be illustrated later (Figure S5). While applying an anodic potential under 0.6 M NaCl, the Co K-edge spectra of the $Ru_{0.09}Co_{2.91}O_4$ NPs showed a positive shift with increasing applied potential from the OCP to 1.4 V (vs Ag/AgCl), whereas those of HT-Co_3O_4 NPs barely shifted (Figure 3a,b). However, despite the increased Co oxidation state

https://doi.org/10.1021/acsomega.3c04525
ACS Omega 2023, 8, 35034−35043

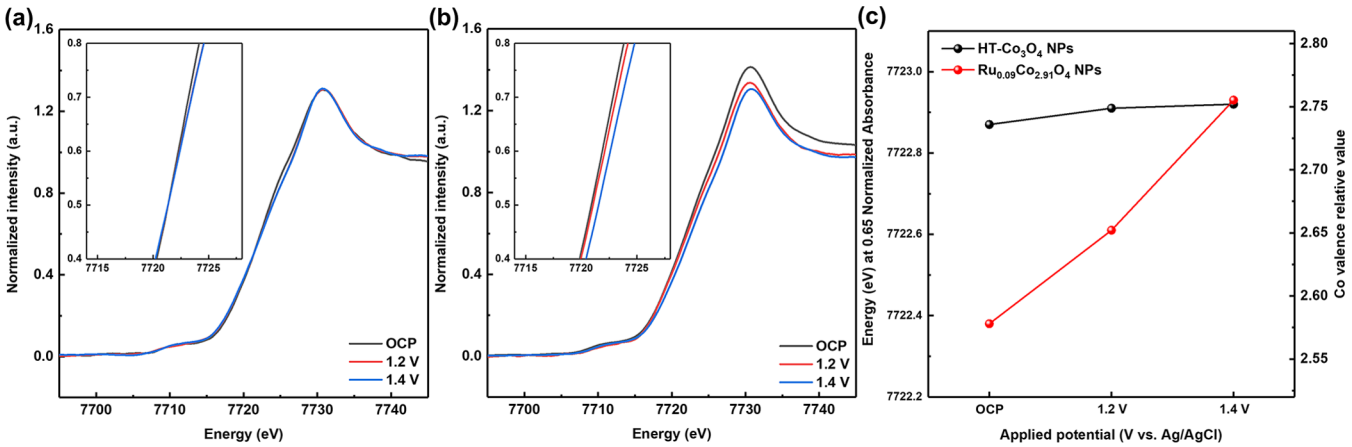

Figure 3. In situ Co K-edge XANES spectra of (a) hydrothermal Co_3O_4 (HT-Co_3O_4) NPs and (b) $Ru_{0.09}Co_{2.91}O_4$ NPs under 0.6 M NaCl (the insets show the enlarged edge regions). (c) Changes in the Co valence of the HT-Co_3O_4 NPs and $Ru_{0.09}Co_{2.91}O_4$ NPs with the applied potential.

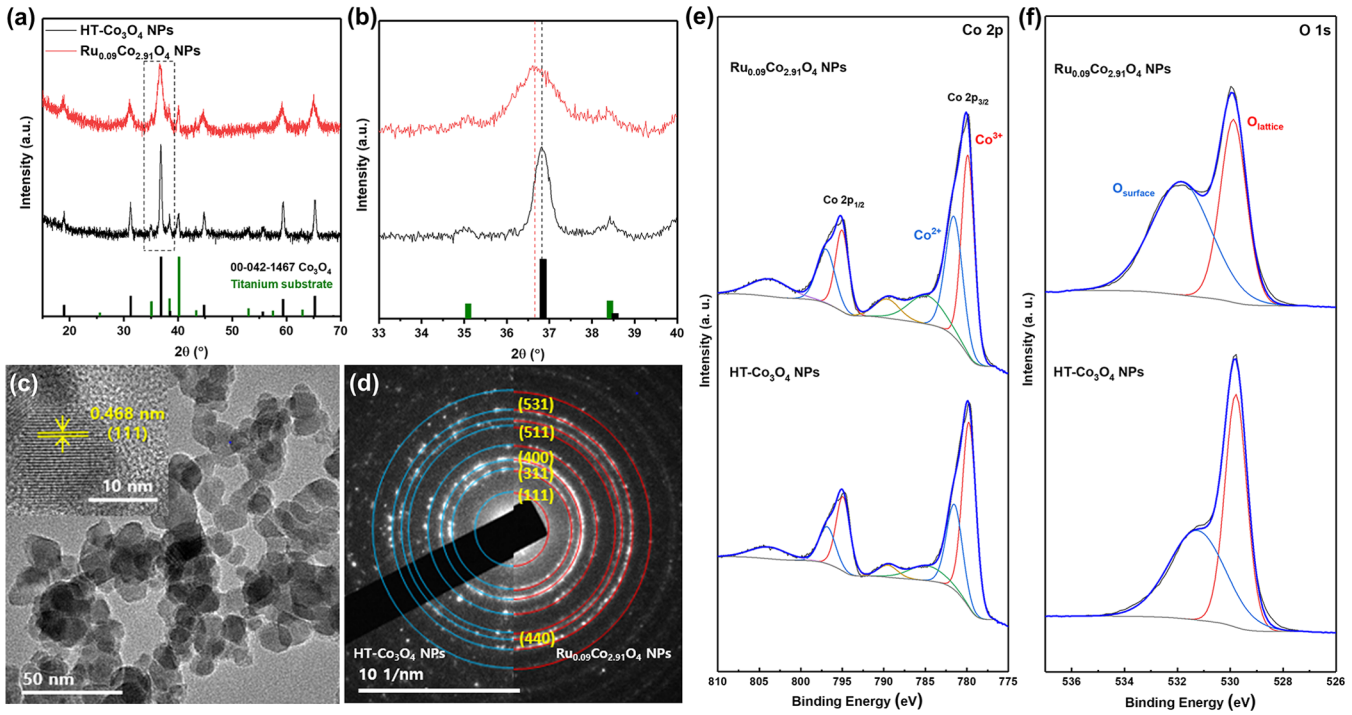

Figure 4. (a) XRD patterns for hydrothermal Co_3O_4 (HT-Co_3O_4) NPs and $Ru_{0.09}Co_{2.91}O_4$ NPs. (b) Enlarged patterns from the dotted box. (c) TEM and HRTEM (inset) images of the $Ru_{0.09}Co_{2.91}O_4$ NPs. (d) Comparison of the SAED patterns for the HT-Co_3O_4 NPs and $Ru_{0.09}Co_{2.91}O_4$ NPs. (e) Co 2p and (f) O 1s XPS spectra of the HT-Co_3O_4 NPs and $Ru_{0.09}Co_{2.91}O_4$ NPs.

during catalysis by the $Ru_{0.09}Co_{2.91}O_4$ NPs, the Co oxidation state did not exceed 3.0 in either case, indicating that high-valent Co(IV) species attributed to adsorbed hydroxyl ions or water molecules were not generated during the CER catalytic cycle (Figure 3c). This indicates that the surfaces of the cobalt atoms were dominantly covered by chlorine ions during the CER. Combined with the electrokinetic and in situ XANES analyses, the overall CER mechanism for the HT-Co_3O_4 NPs and $Ru_{0.09}Co_{2.91}O_4$ NPs at neutral pH was determined to be the Krishtalik mechanism, in which the RDS is the second discharging process generating the adsorbed Cl^+ species. This result was consistent with the mechanism previously proposed for the HI-Co_3O_4 NPs[15] and distinct from that of the Co_3O_4 catalyst in acidic pH, which form an adsorbed oxygenated intermediate.[44] In conclusion, we elucidated that the Ru-incorporated Co_3O_4 NPs exhibited much higher catalytic activity than the HT-Co_3O_4 NPs even though the overall reaction mechanism remained unchanged.

3.4. Material Characterization of the $Ru_xCo_{3-x}O_4$ NPs.

The structural changes of Co_3O_4 induced by the Ru dopant were characterized by XRD, TEM, and XPS analyses to investigate the enhanced CER activity caused by Ru incorporation. As shown in Figure 4a, the XRD patterns for the HT-Co_3O_4 NPs and $Ru_{0.09}Co_{2.91}O_4$ NPs were well matched with that of the cubic Co_3O_4 structure (JCPDS No. 00-042-1467). The $Ru_{0.09}Co_{2.91}O_4$ NPs showed lower crystallinity than the HT-Co_3O_4 NPs, and no other phases, such as RuO_2, were observed. The magnified image (Figure 4b) clearly suggests a negative shift after Ru doping due to changes in the lattice parameters. The altered lattice parameters were ascribed

https://doi.org/10.1021/acsomega.3c04525
ACS Omega 2023, 8, 35034−35043

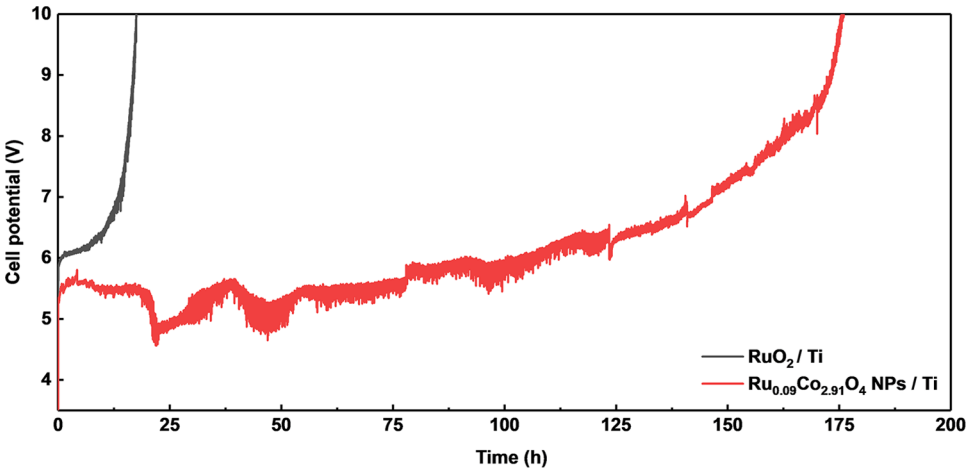

Figure 5. Long-term stability of $Ru_{0.09}Co_{2.91}O_4$ NPs and RuO_2 determined by chronopotentiometry at 500 mA/cm^2 under 0.6 M NaCl.

to insertion of a Ru^{4+} species (0.062 nm) at the octahedral Co^{3+} sites (0.0545 nm). The gradual negative shifts of the diffraction peaks with increasing Ru content ceased when the Ru mole fraction exceeded 3.13% ($Ru_{0.09}Co_{2.91}O_4$ NPs), indicating that excess Ru was not incorporated into the Co_3O_4 lattice (Figure S6). Considering the XRD results and aforementioned CER activity of the $Ru_xCo_{3-x}O_4$ NPs, it was understood that when the Ru ratio reaches 3.13%, Ru is homogeneously coordinated in octahedral sites in Co_3O_4 to the maximum and catalytic performance of the $Ru_xCo_{3-x}O_4$ NPs significantly improved.

Figure 4c illustrates TEM images of the $Ru_{0.09}Co_{2.91}O_4$ NPs, which showed no apparent differences with the morphology and size of the HT-Co_3O_4 NPs. On the other hand, the selected-area electron diffraction (SAED) pattern exhibited coherent ring radius decreases in all of the Co_3O_4 planes after Ru substitution; this indicates an increase in the interplanar spacing after Ru incorporation, which was consistent with the aforementioned XRD results (Figure 4d). The high-angle annular dark-field scanning transmission electron microscopic (HAADF-STEM) images and elemental mapping images of the HT-Co_3O_4 NPs and $Ru_{0.09}Co_{2.91}O_4$ NPs revealed that the Ru species were evenly distributed after Ru doping of the HT-Co_3O_4 NPs (Figure S7).

The surface oxidation and electronic states were investigated by XPS. In the Co 2p spectra (Figure 4e), the main peaks for HT-Co_3O_4 NPs indicated binding energies of 794.85 and 779.75 eV, and these were assigned to Co $2p_{1/2}$ and Co $2p_{3/2}$, respectively; these were positively shifted due to changes in the Co electronic state with the introduction of Ru into the Co_3O_4 lattice. Each peak was fitted with the appropriate Co oxidation state, and the average Co valence was calculated by integrating the area under the fitted curve. The relative ratio of Co^{3+}/Co^{2+} decreases from 2.12 to 1.40, resulting in the decrease of the average Co oxidation state from 2.68 to 2.58, which indicates that Co^{2+} was formed due to substitution of the Ru^{4+} ions into the octahedral Co^{3+} sites. Figure 4f represents the surface properties of the oxygen species in the HT-Co_3O_4 NPs and the $Ru_{0.09}Co_{2.91}O_4$ NPs. The peaks indicating binding energy of 529.80−529.97 eV were characteristic of lattice oxygen (O_{latt}), and the second peaks located at 531.32−531.94 eV were ascribed to nonstoichiometric surface oxygen species (O_{sur}).[45] It was observed that the relative ratio of O_{sur}/O_{latt} estimated from the peaks was the area significantly increased by Ru substitution, implying that Ru−O−Co species induced structural disorder in the Co_3O_4 lattice and increased the number of surface oxygens.[46] On the other hand, these broad shoulder peaks were also known to originate from oxygen defects.[47,48] Based on this interpretation, it was concluded that oxygen vacancies were generated during the Ru doping process, which exposed more internal active sites and accelerated the electrochemical kinetics. In the Ru 3p XPS spectra, the peaks at 463.6 and 485.9 eV corresponded to Ru^{4+}, while those at 462.1 and 484.5 eV indicated Ru^0.[49] Thus, the average Ru oxidation state in the $Ru_xCo_{3-x}O_4$ NPs was calculated to be close to 4.0. The Ru 3d XPS spectra corroborated that Ru(IV) ions were inserted into the Co_3O_4 lattice. The peak at 282.0 eV was assigned to Ru^{4+}, whereas the peak at a lower binding energy of 281.2 eV was related to Ru^{3+} (Figure S8).[50]

3.5. Long-Term Stability Tests of the $Ru_xCo_{3-x}O_4$ NPs.

The need for long-term stability under a high current density constitutes a major challenge for practical application of electrocatalysts.[51] Typically, deactivation of the electrode is closely related to the composition of the active layer and the surface morphology of the catalyst film. The surface cracks caused by tensile stress during annealing facilitate the penetration of the electrolyte through the active catalyst layer, thereby resulting in passivation of the insulating layer.[52,53] Besides, the bubbles formed at the cracks during harsh electrolysis lead to deterioration of the catalyst adhesion and mechanical detachment.[54] Hence, to obtain a uniform and compact catalyst film that is highly resistant to mechanical failure and electrolyte penetration, we carefully controlled several parameters during fabrication of the catalyst layer, such as the solvent for the catalyst ink, the deposition technique, and the annealing temperature. An IPA and water mixture was employed as the solvent, and layer-by-layer brush-coating with drying step at 500 °C was applied, which led to the formation of uniform surface morphology. In addition, the annealing temperature was increased from 300 to 500 °C to achieve better adhesion and a higher mechanical strength. The SEM images in Figure S9 show that the $Ru_{0.09}Co_{2.91}O_4$ NP film prepared via layer-by-layer brush-coating exhibited a homogeneous surface with fewer cracks than the that of prepared by drop-coating. To verify the effect of the change of annealing temperature from 300 to 500 °C on CER mechanistic pathway, we performed a comparative analysis of the Tafel slope and in

https://doi.org/10.1021/acsomega.3c04525
ACS Omega 2023, 8, 35034−35043

situ XANES according to annealing temperature (Figure S10). The Tafel slope of the $Ru_{0.09}Co_{2.91}O_4$ NPs annealed at 500 °C was estimated to be 48 mV/dec, which is similar to that of the 300 °C condition (42 mV/dec), indicating that RDS did not change with increase of the thermal treatment temperature. Besides, the in situ Co K-edge XANES spectra of $Ru_{0.09}Co_{2.91}O_4$ NPs showed similar behavior of oxidation-state variation of Co for the two different annealing conditions, suggesting that high-valent Co(IV) species were not formed during CER regardless of the annealing condition. Based on these results, we confirmed that the mechanistic pathway of the $Ru_{0.09}Co_{2.91}O_4$ NPs was not altered by change of the annealing temperature.

The long-term lifetimes of the $Ru_{0.09}Co_{2.91}O_4$ NPs and RuO_2 electrodes were examined at a constant current density of 500 mA/cm^2, which is comparable to the electrochlorination current densities used in commercial processes (Figure 5).[1] The potential of the $Ru_{0.09}Co_{2.91}O_4$ NP electrode increased slowly for up to 150 h, and then it exhibited a sharp rise indicating the failure of the electrode. The time required to reach 10 V with the $Ru_{0.09}Co_{2.91}O_4$ NP electrode was 175 h under a current density of 500 mA/cm^2. On the other hand, the RuO_2 electrode, which exhibited a lifetime of 17 h, underwent a drastic increase in the potential from initial stage, which was attributed to severe dissolution of Ru at the high anodic potential.[55] Time-dependent current efficiency measurement of the $Ru_{0.09}Co_{2.91}O_4$ NPs showed consistent high selectivity for chlorine generation during long-term lifetime test (Figure S11). The high durability of the $Ru_{0.09}Co_{2.91}O_4$ NP electrode comparable with commercial CER electrodes suggests that the $Ru_xCo_{3-x}O_4$ NPs could be viable material for industrial level of electrochlorination.

To investigate the structure and electronic-state change of the $Ru_{0.09}Co_{2.91}O_4$ NPs after the long-term lifetime test, TEM and XPS analyses were conducted. As illustrated in Figure S12, before and after electrochemical operation, the $Ru_{0.09}Co_{2.91}O_4$ NPs exhibited similar morphology and average size (8−12 nm). However, STEM-EDX mapping images revealed that average Ru ratio in the $Ru_{0.09}Co_{2.91}O_4$ NPs decreased from 3.69 to 2.52 atom % ascribed to anodic dissolution of Ru (Figure S13). After reaction, XPS Co 2p spectra exhibited similar peak shapes and positions of Co to those of the pristine $Ru_{0.09}Co_{2.91}O_4$ NPs, resulting in similar Co^{3+}/Co^{2+} ratio of 1.38. Although the remaining Co showed similar oxidation state, the overall peak intensity of Co significantly decreased, suggesting degradation of a notable amount of the catalyst during electrolysis. After lifetime measurement, oxygen concentration in the lattice structure decreased, meanwhile contribution of surface oxygen species, including hydroxyl species and adsorbed water molecule, increased. This result implies that competitive water oxidation resulted in hydroxylation of the surface.[56,57] In addition, the dissolution of Ru species in the $Ru_{0.09}Co_{2.91}O_4$ NPs can lead to increase in nonstoichiometric oxygen concentration (Figure S14). Both Ru 3p and 3d XPS spectra demonstrated that peak intensity of Ru species clearly decreased, indicating severe Ru dissolution during reaction. Besides, a characteristic titanium peak appeared at 458.5 eV in Ru 3p spectra due to degradation of the catalyst layer and exposure of the underlying Ti substrate (Figure S15). The post-mortem analyses after long-term operation suggest that anodic dissolution under high current density is the major deactivation factor for the $Ru_{0.09}Co_{2.91}O_4$ NPs. However, further study is required to point out the exact deactivation mechanism for the $Ru_{0.09}Co_{2.91}O_4$ NPs.

4. CONCLUSIONS

In summary, we synthesized Co_3O_4 NPs as CER electrocatalysts via a facile and cost-effective hydrothermal method and proposed an efficient scheme for Ru incorporation into the HT-Co_3O_4 NPs. The $Ru_{0.09}Co_{2.91}O_4$ NPs showed superior activity in the CER compared to RuO_2 and commercial DSA under neutral conditions. A series of characterizations of the $Ru_{0.09}Co_{2.91}O_4$ NPs showed that Ru^{4+} ions were homogeneously substituted into the octahedral Co^{3+} sites of the Co_3O_4 spinel structure, which led to structural distortions and electronic-state modulation of the Co_3O_4 NPs. The electrokinetic and in situ XANES analyses suggested that both HT-Co_3O_4 NPs and $Ru_xCo_{3-x}O_4$ NPs follow the identical CER mechanism, where the second discharging step that forms the adsorbed Cl^+ species is the RDS. Finally, we achieved high stability with the $Ru_{0.09}Co_{2.91}O_4$ NP electrode with a lifetime above 150 h at a current density of 500 mA/cm^2 via optimization of the catalyst layer fabrication process. We expect that our $Ru_xCo_{3-x}O_4$ NPs, with their robust catalytic properties as well as their scalability, may be extended into various other electrochemical catalytic applications.

■ ASSOCIATED CONTENT

Supporting Information

The Supporting Information is available free of charge at https://pubs.acs.org/doi/10.1021/acsomega.3c04525.

XRD patterns, electrochemical characterization results, current efficiency measurements, XANES spectra, XPS spectra, and EDX elemental mapping images for the HT-Co_3O_4 NPs and $Ru_{0.09}Co_{2.91}O_4$ NPs (PDF)

■ AUTHOR INFORMATION

Corresponding Author

Ki Tae Nam − *Department of Materials Science and Engineering, Seoul National University, Seoul 08826, Republic of Korea; Soft Foundry, Seoul National University, Seoul 08826, Republic of Korea;* orcid.org/0000-0001-6353-8877; Email: nkitae@snu.ac.kr

Authors

Won Il Choi − *Department of Materials Science and Engineering, Seoul National University, Seoul 08826, Republic of Korea*

Seungwoo Choi − *Department of Materials Science and Engineering, Seoul National University, Seoul 08826, Republic of Korea; Soft Foundry, Seoul National University, Seoul 08826, Republic of Korea*

Mani Balamurugan − *Department of Materials Science and Engineering, Seoul National University, Seoul 08826, Republic of Korea; Soft Foundry, Seoul National University, Seoul 08826, Republic of Korea;* orcid.org/0000-0002-9256-6591

Sunghak Park − *Department of Materials Science and Engineering, Seoul National University, Seoul 08826, Republic of Korea;* orcid.org/0000-0001-9394-4833

Kang Hee Cho − *Department of Materials Science and Engineering, Seoul National University, Seoul 08826, Republic of Korea*

https://doi.org/10.1021/acsomega.3c04525
ACS Omega 2023, 8, 35034−35043

Hongmin Seo − *Department of Materials Science and Engineering, Seoul National University, Seoul 08826, Republic of Korea*

Heonjin Ha − *Department of Materials Science and Engineering, Seoul National University, Seoul 08826, Republic of Korea*

Complete contact information is available at: https://pubs.acs.org/10.1021/acsomega.3c04525

Notes

The authors declare no competing financial interest.

■ ACKNOWLEDGMENTS

This research was supported by Creative Materials Discovery Program through the National Research Foundation of Korea (NRF) funded by the Ministry of Science and ICT (NRF-2017M3D1A1039377 and 2017M3D1A1039378); Korea Environment Industry & Technology Institute (KEITI) through Ecological Imitation-based Environmental Pollution Management Technology Development Project, funded by Korea Ministry of Environment (MOE) (2021002800013); and Research Institute of Advanced Materials (RIAM) and Soft Foundry at Seoul National University.

■ REFERENCES

(1) Karlsson, R. K. B.; Cornell, A. Selectivity between Oxygen and Chlorine Evolution in the Chlor-Alkali and Chlorate Processes. *Chem. Rev.* **2016**, *116*, 2982−3028.

(2) Vos, J. G.; Liu, Z.; Speck, F. D.; Perini, N.; Fu, W.; Cherevko, S.; Koper, M. T. M. Selectivity Trends Between Oxygen Evolution and Chlorine Evolution on Iridium-Based Double Perovskites in Acidic Media. *ACS Catal.* **2019**, *9*, 8561−8574.

(3) Tsolaki, E.; Diamadopoulos, E. Technologies for ballast water treatment: a review. *J. Chem. Technol. Biotechnol.* **2010**, *85*, 19−32.

(4) Harrison, J. A.; Caldwell, D. L.; White, R. E. Electrocatalysis and the chlorine evolution reaction. *Electrochim. Acta* **1983**, *28*, 1561−1568.

(5) Harrison, J. A.; Caldwell, D. L.; White, R. E. Electrocatalysis and the chlorine evolution reaction—II. Comparison of anode materials. *Electrochim. Acta* **1984**, *29*, 203−209.

(6) Trasatti, S. Electrocatalysis in the anodic evolution of oxygen and chlorine. *Electrochim. Acta* **1984**, *29*, 1503−1512.

(7) Trasatti, S. Electrocatalysis: understanding the success of DSA. *Electrochim. Acta* **2000**, *45*, 2377−2385.

(8) Takasu, Y.; Sugimoto, W.; Nishiki, Y.; Nakamatsu, S. Structural analyses of RuO2−TiO2/Ti and IrO2−RuO2−TiO2/Ti anodes used in industrial chlor-alkali membrane processes. *J. Appl. Electrochem.* **2010**, *40*, 1789−1795.

(9) Arikawa, T.; Murakami, Y.; Takasu, Y. Simultaneous determination of chlorine and oxygen evolving at RuO2/Ti and RuO2−TiO2/Ti anodes by differential electrochemical mass spectroscopy. *J. Appl. Electrochem.* **1998**, *28*, 511−516.

(10) Moreno-Hernandez, I. A.; Brunschwig, B. S.; Lewis, N. S. Crystalline nickel, cobalt, and manganese antimonates as electrocatalysts for the chlorine evolution reaction. *Energy Environ. Sci.* **2019**, *12*, 1241−1248.

(11) Alavijeh, M. M.; Habibzadeh, S.; Roohi, K.; Keivanimehr, F.; Naji, L.; Ganjali, M. R. A selective and efficient precious metal-free electrocatalyst for chlorine evolution reaction: An experimental and computational study. *J. Chem. Eng.* **2021**, *421*, No. 127785.

(12) Zhu, X.; Wang, P.; Wang, Z.; Liu, Y.; Zheng, Z.; Zhang, Q.; Zhang, X.; Dai, Y.; Whangbo, M.-H.; Huang, B. Co3O4 nanobelt arrays assembled with ultrathin nanosheets as highly efficient and stable electrocatalysts for the chlorine evolution reaction. *J. Mater. Chem. A* **2018**, *6*, 12718−12723.

(13) Lim, T.; Jung, G. Y.; Kim, J. H.; Park, S. O.; Park, J.; Kim, Y.-T.; Kang, S. J.; Jeong, H. Y.; Kwak, S. K.; Joo, S. H. Atomically dispersed Pt−N4 sites as efficient and selective electrocatalysts for the chlorine evolution reaction. *Nat. Commun.* **2020**, *11*, No. 412.

(14) Jin, K.; Seo, H.; Hayashi, T.; Balamurugan, M.; Jeong, D.; Go, Y. K.; Hong, J. S.; Cho, K. H.; Kakizaki, H.; Bonnet-Mercier, N.; et al. Mechanistic Investigation of Water Oxidation Catalyzed by Uniform, Assembled MnO Nanoparticles. *J. Am. Chem. Soc.* **2017**, *139*, 2277−2285.

(15) Ha, H.; Jin, K.; Park, S.; Lee, K.-G.; Cho, K. H.; Seo, H.; Ahn, H.-Y.; Lee, Y. H.; Nam, K. T. Highly Selective Active Chlorine Generation Electrocatalyzed by Co3O4 Nanoparticles: Mechanistic Investigation through in Situ Electrokinetic and Spectroscopic Analyses. *J. Phys. Chem. Lett.* **2019**, *10*, 1226−1233.

(16) Zhang, S. L.; Guan, B. Y.; Lu, X. F.; Xi, S.; Du, Y.; Lou, X. W. Metal Atom-Doped Co3O4 Hierarchical Nanoplates for Electrocatalytic Oxygen Evolution. *Adv. Mater.* **2020**, *32*, No. 2002235.

(17) Park, S.; Jin, K.; Lim, H. K.; Kim, J.; Cho, K. H.; Choi, S.; Seo, H.; Lee, M. Y.; Lee, Y. H.; Yoon, S.; et al. Spectroscopic capture of a low-spin Mn(IV)-oxo species in Ni−Mn3O4 nanoparticles during water oxidation catalysis. *Nat. Commun.* **2020**, *11*, No. 5230.

(18) Zhang, H.; Yu, L.; Chen, T.; Zhou, W.; Lou, X. W. Surface Modulation of Hierarchical MoS2 Nanosheets by Ni Single Atoms for Enhanced Electrocatalytic Hydrogen Evolution. *Adv. Funct. Mater.* **2018**, *28*, No. 1807086.

(19) Fragal, V. H.; Fragal, E. H.; Zhang, T.; Huang, X.; Cellet, T. S. P.; Pereira, G. M.; Jitianu, A.; Rubira, A. F.; Silva, R.; Asefa, T. Deriving Efficient Porous Heteroatom-Doped Carbon Electrocatalysts for Hydrazine Oxidation from Transition Metal Ions-Coordinated Casein. *Adv. Funct. Mater.* **2019**, *29*, No. 1808486.

(20) Wang, X.; Sun, P.; Lu, H.; Tang, K.; Li, Q.; Wang, C.; Mao, Z.; Ali, T.; Yan, C. Aluminum-Tailored Energy Level and Morphology of Co3−xAlxO4 Porous Nanosheets toward Highly Efficient Electrocatalysts for Water Oxidation. *Small* **2019**, *15*, No. 1804886.

(21) Duan, Y.; Sun, S.; Sun, Y.; Xi, S.; Chi, X.; Zhang, Q.; Ren, X.; Wang, J.; Ong, S. J. H.; Du, Y.; et al. Mastering Surface Reconstruction of Metastable Spinel Oxides for Better Water Oxidation. *Adv. Mater.* **2019**, *31*, No. 1807898.

(22) Liu, Y.; Ying, Y.; Fei, L.; Liu, Y.; Hu, Q.; Zhang, G.; Pang, S. Y.; Lu, W.; Mak, C. L.; Luo, X.; et al. Valence Engineering via Selective Atomic Substitution on Tetrahedral Sites in Spinel Oxide for Highly Enhanced Oxygen Evolution Catalysis. *J. Am. Chem. Soc.* **2019**, *141*, 8136−8145.

(23) Wu, T.; Sun, S.; Song, J.; Xi, S.; Du, Y.; Chen, B.; Sasangka, W. A.; Liao, H.; Gan, C. L.; Scherer, G. G.; et al. Iron-facilitated dynamic active-site generation on spinel CoAl2O4 with self-termination of surface reconstruction for water oxidation. *Nat. Catal.* **2019**, *2*, 763−772.

(24) Zeradjanin, A. R.; Menzel, N.; Strasser, P.; Schuhmann, W. Role of Water in the Chlorine Evolution Reaction at RuO2-Based Electrodes—Understanding Electrocatalysis as a Resonance Phenomenon. *ChemSusChem* **2012**, *5*, 1897−1904.

(25) Li, W.; Feng, B.; Yi, L.; Li, J.; Hu, W. Highly Efficient Alkaline Water Splitting with Ru-Doped Co−V Layered Double Hydroxide Nanosheets as a Bifunctional Electrocatalyst. *ChemSusChem* **2021**, *14*, 730−737.

(26) Guo, B.; Ma, R.; Li, Z.; Luo, J.; Yang, M.; Wang, J. Dual-doping of ruthenium and nickel into Co3O4 for improving the oxygen evolution activity. *Mater. Chem. Front.* **2020**, *4*, 1390−1396.

(27) Liu, H.; Li, X.; Ge, L.; Peng, C.; Zhu, L.; Zou, W.; Chen, J.; Wu, Q.; Zhang, Y.; Huang, H.; et al. Accelerating hydrogen evolution in Ru-doped FeCoP nanoarrays with lattice distortion toward highly efficient overall water splitting. *Catal. Sci. Technol.* **2020**, *10*, 8314−8324.

(28) Wang, C.; Qi, L. Heterostructured Inter-Doped Ruthenium−Cobalt Oxide Hollow Nanosheet Arrays for Highly Efficient Overall Water Splitting. *Angew. Chem., Int. Ed.* **2020**, *59*, 17372−17377.

(29) Vadimsky, R. G.; Frankenthal, R. P.; Thompson, D. E. Ru and RuO2 as electrical contact materials: Preparation and environmental interactions. *J. Electrochem. Soc.* **1979**, *126*, 2017−2023.
(30) Dong, Y.; He, K.; Yin, L.; Zhang, A. A facile route to controlled synthesis of Co3O4 nanoparticles and their environmental catalytic properties. *Nanotechnology* **2007**, *18*, No. 435602.
(31) Mansournia, M.; Rakhshan, N. Amine ligand-based hydrothermal synthesis of Co3O4 nanoparticles, characterization and magnetic study. *J. Mol. Struct.* **2016**, *1125*, 714−720.
(32) Melsheimer, J.; Ziegler, D. The oxygen electrode reaction in acid solutions on RuO2 electrodes prepared by the thermal decomposition method. *Thin Solid Films* **1988**, *163*, 301−308.
(33) Lee, C. W.; Hong, J. S.; Yang, K. D.; Jin, K.; Lee, J. H.; Ahn, H.-Y.; Seo, H.; Sung, N.-E.; Nam, K. T. Selective Electrochemical Production of Formate from Carbon Dioxide with Bismuth-Based Catalysts in an Aqueous Electrolyte. *ACS Catal.* **2018**, *8*, 931−937.
(34) Grzelczak, M.; Zhang, J.; Pfrommer, J.; Hartmann, J.; Driess, M.; Antonietti, M.; Wang, X. Electro- and Photochemical Water Oxidation on Ligand-free Co3O4 Nanoparticles with Tunable Sizes. *ACS Catal.* **2013**, *3*, 383−388.
(35) Kim, Y.; Park, J. H.; Kim, J. G.; Noh, Y.; Kim, Y.; Han, H.; Kim, W. B. Ruthenium Oxide Incorporated One-Dimensional Cobalt Oxide Composite Nanowires as Lithium−Oxygen Battery Cathode Catalysts. *ChemCatChem* **2017**, *9*, 3554−3562.
(36) Rakhi, R. B.; Chen, W.; Hedhili, M. N.; Cha, D.; Alshareef, H. N. Enhanced Rate Performance of Mesoporous Co3O4 Nanosheet Supercapacitor Electrodes by Hydrous RuO2 Nanoparticle Decoration. *ACS Appl. Mater. Interfaces* **2014**, *6*, 4196−4206.
(37) Dubal, D. P.; Chodankar, N. R.; Holze, R.; Kim, D.-H.; Gomez-Romero, P. Ultrathin Mesoporous RuCo2O4 Nanoflakes: An Advanced Electrode for High-Performance Asymmetric Supercapacitors. *ChemSusChem* **2017**, *10*, 1771−1782.
(38) Ambare, R. C.; Bharadwaj, S. R.; Lokhande, B. J. Non-aqueous route spray pyrolyzed Ru:Co3O4 thin electrodes for supercapacitor application. *Appl. Surf. Sci.* **2015**, *349*, 887−896.
(39) Seo, H.; Jin, K.; Park, S.; Cho, K. H.; Ha, H.; Lee, K.-G.; Lee, Y. H.; Nguyen, D. T.; Randriamahazaka, H.; Lee, J.-S.; Nam, K. T. Mechanistic Investigation with Kinetic Parameters on Water Oxidation Catalyzed by Manganese Oxide Nanoparticle Film. *ACS Sustainable Chem. Eng.* **2019**, *7*, 10595−10604.
(40) Lee, M. Y.; Ha, H.; Cho, K. H.; Seo, H.; Park, S.; Lee, Y. H.; Kwon, S.-J.; Lee, T.-W.; Nam, K. T. Importance of Interfacial Band Structure between the Substrate and Mn3O4 Nanocatalysts during Electrochemical Water Oxidation. *ACS Catal.* **2020**, *10*, 1237−1245.
(41) Burke, L. D.; McCarthy, M. M. *Modification of the Electronic Transfer Properties of Co3O4 as Required for Its Use in 1DSA-Type Anodes*; Electrochemical Society, 1987; Vol. *2*, p 343.
(42) Boggio, R.; Carugati, A.; Trasatti, S. Electrochemical surface properties of Co3O4 electrodes. *J. Appl. Electrochem.* **1987**, *17*, 828−840.
(43) Shinagawa, T.; Garcia-Esparza, A. T.; Takanabe, K. Insight on Tafel slopes from a microkinetic analysis of aqueous electrocatalysis for energy conversion. *Sci. Rep.* **2015**, *5*, No. 13801.
(44) Boggio, R.; Carugati, A.; Lodi, G.; Trasatti, S. Mechanistic study of C12 evolution at Ti-supported Co3O4 anodes. *J. Appl. Electrochem.* **1985**, *15*, 335−349.
(45) Weidler, N.; Paulus, S.; Schuch, J.; Klett, J.; Hoch, S.; Stenner, P.; Maljusch, A.; Brötz, J.; Wittich, C.; Kaiser, B.; Jaegermann, W. CoOx thin film deposited by CVD as efficient water oxidation catalyst: change of oxidation state in XPS and its correlation to electrochemical activity. *Phys. Chem. Chem. Phys.* **2016**, *18*, 10708−10718.
(46) Lao, Y.; Zhu, N.; Jiang, X.; Zhao, J.; Dai, Q.; Wang, X. Effect of Ru on the activity of Co3O4 catalysts for chlorinated aromatics oxidation. *Catal. Sci. Technol.* **2018**, *8*, 4797−4811.
(47) Cai, Z.; Bi, Y.; Hu, E.; Liu, W.; Dwarica, N.; Tian, Y.; Li, X.; Kuang, Y.; Li, Y.; Yang, X.-Q.; et al. Single-Crystalline Ultrathin Co3O4 Nanosheets with Massive Vacancy Defects for Enhanced Electrocatalysis. *Adv. Energy Mater.* **2018**, *8*, No. 1701694.
(48) Yin, G.; Yuan, X.; Du, X.; Zhao, W.; Bi, Q.; Huang, F. Efficient Reduction of CO2 to CO Using Cobalt−Cobalt Oxide Core−Shell Catalysts. *Chem. - Eur. J.* **2018**, *24*, 2157−2163.
(49) Wang, H.; Li, X.; Ruan, Q.; Tang, J. Ru and RuOx decorated carbon nitride for efficient ammonia photosynthesis. *Nanoscale* **2020**, *12*, 12329−12335.
(50) Laha, S.; Lee, Y.; Podjaski, F.; Weber, D.; Duppel, V.; Schoop, L. M.; Pielnhofer, F.; Scheurer, C.; Müller, K.; Starke, U.; et al. Ruthenium Oxide Nanosheets for Enhanced Oxygen Evolution Catalysis in Acidic Medium. *Adv. Energy Mater.* **2019**, *9*, No. 1803795.
(51) Wang, Y.; Liu, Y.; Wiley, D.; Zhao, S.; Tang, Z. Recent advances in electrocatalytic chloride oxidation for chlorine gas production. *J. Mater. Chem. A* **2021**, *9*, 18974−18993.
(52) Chen, R.; Trieu, V.; Zeradjanin, A. R.; Natter, H.; Teschner, D.; Kintrup, J.; Bulan, A.; Schuhmann, W.; Hempelmann, R. Microstructural impact of anodic coatings on the electrochemical chlorine evolution reaction. *Phys. Chem. Chem. Phys.* **2012**, *14*, 7392−7399.
(53) Zeng, X.; Zhang, M.; Wang, X.; Chen, X.; Su, X.; Tang, W. Effects of Sn content on Ti/RuO2−SnO2−TiO2 anodes used in the generation of electrolyzed oxidizing water. *J. Electroanal. Chem.* **2012**, *677−680*, 133−138.
(54) Kariman, A.; Marshall, A. T. Improving the stability of DSA electrodes by the addition of TiO2 nanoparticles. *J. Electrochem. Soc.* **2019**, *166*, E248−E251.
(55) Kasian, O.; Geiger, S.; Stock, P.; Polymeros, G.; Breitbach, B.; Savan, A.; Ludwig, A.; Cherevko, S.; Mayrhofer, K. J. J. On the origin of the improved ruthenium stability in RuO2−IrO2 mixed oxides. *J. Electrochem. Soc.* **2016**, *163*, F3099−F3104.
(56) Lim, H. W.; Cho, D. K.; Park, J. H.; Ji, S. G.; Ahn, Y. J.; Kim, J. Y.; Lee, C. W. Rational Design of Dimensionally Stable Anodes for Active Chlorine Generation. *ACS Catal.* **2021**, *11*, 12423−12432.
(57) Malik, A. S.; Liu, T. F.; Dupuis, M.; Li, R. G.; Li, C. Water Oxidation on TiO2: A Comparative DFT Study of 1e(-), 2e(-), and 4e(-) Processes on Rutile, Anatase, and Brookite. *J. Phys. Chem. C* **2020**, *124*, 8094−8100.

https://doi.org/10.1021/acsomega.3c04525
ACS Omega 2023, 8, 35034−35043